Investigation into the effect of Si doping on the cell symmetry and performance of $Sr_{1-y}Ca_yFeO_{3-\delta}$ SOFC cathode materials

Porras-vazquez, Jose M.; Smith, R.i.; Slater, Peter R.

[Link to publication on Research at Birmingham portal](#)

Investigation into the effect of Si doping on the cell symmetry and performance of $Sr_{1-y}Ca_yFeO_{3-\delta}$ SOFC cathode materials

Jose M. Porras-Vazquez [a,*], R.I. Smith [b], Peter R. Slater [a,*]

[a] School of Chemistry, University of Birmingham, Birmingham, B15 2TT, UK
[b] ISIS Facility, Rutherford Appleton Laboratory, Harwell Oxford, Didcot, OX11 0QX, UK

ABSTRACT

In this paper we report the successful incorporation of silicon into $Sr_{1-y}Ca_yFeO_{3-\delta}$ perovskite materials for potential applications as electrode materials for Solid Oxide Fuel Cells. It is observed that Si doping leads to a change from a tetragonal or orthorhombic structure (with partial ordering of oxygen vacancies) to a cubic one (with the oxygen vacancies disordered). The structures of the phases, $SrFe_{0.85}Si_{0.15}O_{3-\delta}$, $Sr_{0.75}Ca_{0.25}Fe_{0.85}Si_{0.15}O_{3-\delta}$ and $Sr_{0.5}Ca_{0.5}Fe_{0.85}Si_{0.15}O_{3-\delta}$, were analysed using neutron powder diffraction. The data confirmed the cubic unit cell, with no long range oxygen vacancy ordering. Conductivity measurements showed an improvement in the conductivity on Si doping, especially for samples with high Ca content. Composite electrodes comprising 50% $Ce_{0.9}Gd_{0.1}O_{1.95}$ and 50% $Sr_{1-y}Ca_y(Fe/Si)O_{3-\delta}$ on dense $Ce_{0.9}Gd_{0.1}O_{1.95}$ pellets were therefore examined in air. An improvement in the area specific resistances (ASR) values is observed for the Si-doped samples with respect to the undoped samples. Thus the results show that silicon can be incorporated into $Sr_{1-y}Ca_yFeO_{3-\delta}$-based materials and can have a beneficial effect on the performance, making them potentially suitable for use as cathode material in Solid Oxide Fuel Cells (SOFC).

© 2014 Elsevier Inc. All rights reserved.

1. Introduction

Perovskite transition metal containing oxides have attracted considerable interest due to potential applications as cathode materials in the field of Solid Oxide Fuel Cells (SOFCs). Traditionally doping strategies for such materials has focused on substitution with cations of similar size, e.g. Sr for La [1–5]. Recently we have investigated an alternative doping strategy consisting of the partial replacement of the octahedral B site cation in perovskite with oxyanion groups. Our doping strategy stems from prior observations on the successful incorporation of oxyanions into perovskite-type cuprate superconductors and related phases [6–14]. This work demonstrated that the perovskite structure can incorporate significant levels of oxyanions (carbonate, borate, nitrate, sulfate, phosphate). In such samples, the C, B, N, P, S of the oxyanion group was shown to reside on the perovskite B cation site, with the oxide ions of this group filling 3 (C, B, N)–4 (P, S) of the available 6 oxide ion positions around this site. Recently we have illustrated the potential of this oxyanion doping strategy in perovskite-type materials with potential for use as electrode materials in solid oxide fuel cells [15–17]. For instance, borate, phosphate and sulphate were successfully incorporated into different cathode materials such as $SrCoO_{3-\delta}$, $La_{1-x}Sr_xCo_{0.8}Fe_{0.2}O_{3-\delta}$, $Ba_{1-x}Sr_xCo_{0.8}Fe_{0.2}O_{3-\delta}$, $CaMnO_3$ and $La_{1-x}Sr_xMnO_3$-type materials, leading to stabilization of high symmetry structures, as well as enhancements of both the electronic conductivity and the electrode performance with respect to the parent compounds.

The introduction of silicate groups is of particular interest, because silica is widely considered a detrimental contaminant of SOFC materials, particularly electrolyte materials, as it has been reported to segregate at the grain boundaries where it forms insulating siliceous phases, lowering the conductivity, such that overall performance is degraded [18–27].

Our preliminary studies on Si incorporation were performed in cobalt-based perovskite electrode materials, showing the successful incorporation of Si into $La_{0.6}Sr_{0.4}Co_{0.8}Fe_{0.2}O_{3-\delta}$ and $Sr_{1-x}Y_xCoO_{3-\delta}$–based materials, with significant results in term of improvements in the conductivity and an enhancement in the stability towards CO_2 [28]. More recently, $Sr_yCa_{1-y}Mn_{1-x}Si_xO_{3-\delta}$ cathode materials have been prepared, and direct evidence for the incorporation of Si into the structure provided for the first time by ^{29}Si NMR [29,30]. In each case, Si doping is shown to enhance the conductivity, which can be attributed to electron doping (driven by the introduction of oxide ion vacancies due to the preference for Si to adopt tetrahedral coordination), as well as a change from a hexagonal (containing face sharing of octahedra) to a cubic perovskite (containing corner sharing of octahedra).

In a recent work we have extended such studies to $SrFeO_{3-\delta}$, which is an interesting material that exhibits both high mixed oxide ionic and high electronic conductivity and therefore can be potentially used in electrochemical devices such as oxygen permeation membranes, and SOFCs [31–33]. Iron cations in this system have a mixed valence state with an average oxidation state between +4 to +3, corresponding to a wide range of oxygen nonstoichiometry. The structure changes from tetragonal to orthorhombic brownmillerite type, as the iron oxidation state reduces to 3+ and hence the composition changes to $SrFeO_{2.5}$, with associated long range ordering of oxide ion vacancies [34–36]. The formation of ordered oxygen vacancies is not favourable for practical applications because it drastically reduces oxide ion conduction, while the oxygen deficiency also results in a decrease in both the mobility and concentration of hole carriers [37,38]. Through Si doping $SrFeO_{3-\delta}$, we were able to stabilize the high symmetry cubic form, even in low oxygen partial pressures, with Mössbauer studies indicating a disproportionation of Fe^{4+} into Fe^{3+} and Fe^{5+}, attributed to the influence of the Si [39]. In the present work we extend our earlier study to the $Sr_{1-y}Ca_yFeO_{3-\delta}$ system, where the Ca substitution increases the distortion of the unit cell over that found in $SrFeO_{3-\delta}$. For $Sr_{1-y}Ca_yFeO_{3-\delta}$, Takeda et al., showed a transition from an orthorhombic cell, at low strontium contents, even under higher $p(O_2)$, to a cubic symmetry at higher strontium contents [40]. In our work, we examine the effect of Si doping on the cell symmetry, conductivity, and cathode performance of such systems. This work is also of relevance to Earth Science, where $(Mg, Fe)SiO_3$, $(Ca, Fe)SiO_3$ and $Ca(Si, Fe)O_{3-x}$ phases have attracted substantial interest due to their accepted presence in the Earth's interior [41–44]. Such phases have been traditionally thought to require very high pressure synthesis conditions, and so the work here, showing the synthesis of a range of Fe and Si containing perovskite at ambient pressure, is of significant relevance to the perovskite chemistry field in general, indicating that the ability of the perovskite structure to accommodate Si is far more widespread than initially believed.

2. Experimental

$SrCO_3$ (Aldrich, 99.9%), $CaCO_3$ (Aldrich, 99%), Fe_2O_3 (Fluka, 99%) and SiO_2 (Aldrich, 99.6%), were used to prepare $Sr_{1-y}Ca_yFe_{1-x}Si_xO_{3-\delta}$ (y=0, 0.25, 0.5, 0.75 and 1; $x \leq 0.20$). The powders were intimately ground and heated initially to 1100 °C for 12 h. They were then ball-milled (350 rpm for 1 h, Fritsch Pulverisette 7 Planetary Mill) and reheated to 1150 °C for a further 12 h. Finally, they were then ball-milled (350 rpm for 1 h) and reheated to 1200 °C for a further 12 h.

Initial phase identification and unit cell parameter determination was carried out by Rietveld profile refinement using powder X-ray diffraction data (XRD) collected on a Bruker D8 diffractometer (Cu $K\alpha_1$ radiation).

For the determination of any possible oxide vacancy ordering, time-of-flight powder neutron diffraction data were collected on the POLARIS diffractometer at the ISIS pulsed neutron source (Rutherford Appleton Laboratory, UK).

Analysis of both the X-ray and neutron diffraction data by the Rietveld method was done using the General Structure Analysis System GSAS [45].

Oxygen contents were estimated from thermogravimetric analysis (Netzsch STA 449 F1 Jupiter Thermal Analyser). Samples were heated at 10 °C min^{-1} to 1200 °C in N_2 and held for 30 min to reduce the Fe oxidation state to 3+, with the original oxygen content and average Fe oxidation state then being determined from the mass loss observed.

Pellets for conductivity measurements were prepared as follows: the powders were first ball-milled (350 rpm for 1 h), before pressing (200 MPa) as pellets and sintering at 1200 °C for 12 h. Four Pt electrodes were attached with Pt paste, and the sample was fired to 800 °C in air for 1 h to ensure bonding to the sample. The samples were then furnace cooled to 350 °C in air and held at this temperature for 12 h to ensure full oxygenation. Finally, their conductivities were measured using the four probe dc method in air.

To elucidate the potential of these materials for use as SOFC cathodes, symmetrical electrodes were coated on both sides of dense $Ce_{0.9}Gd_{0.1}O_{1.95}$ (CGO10, Aldrich) pellets (sintered at 1500 °C for 12 h) using a suspension prepared with a mixture of electrolyte and electrodes (1:1 wt%) and DecofluxTM (WB41, Zschimmer and Schwarz) as binder material. The symmetrical cells were fired at 900 °C for 1 h in air. Afterwards, a Pt-based ink was applied onto the electrodes to produce a current collector layer and finally the pellets were fired at 800 °C for 1 h. Area-specific resistance (ASR) values were then obtained under symmetrical air atmosphere in a two electrode configuration. AC impedance spectra of the electrochemical cells were collected using a HP4912A frequency analyser, at open circuit voltage (OCV), in the 5 Hz–13 MHz frequency range with ac signal amplitude of 100 mV. The spectra were fitted to equivalent circuits using the ZView software [46] which allows an estimation of the resistance and capacitance associated with the different cell contributions.

3. Results and discussion

3.1. Solid solution range

For the $Sr_{1-y}Ca_yFe_{1-x}Si_xO_{3-\delta}$ series (y=0, 0.25, 0.5 and 0.75), single phase samples could be achieved up to 15% silicon substitution, i.e. $x = \leq 0.15$ (Fig. 1). Exceeding this Si content led to the segregation of secondary phases, such as Sr_2SiO_4 (PDF 038-0271). For the Ca-end member, $CaFeO_{3-\delta}$, the samples were only single phase up to x=0.05, with attempts to produce more silicon-rich compositions leading to the segregation of secondary phases, such as Ca_2SiO_4 (PDF 009-0351), and there was no change in the cell symmetry for this series. All the undoped samples showed some degree of oxygen ordering, for instance, the Sr end member (y=0) has a tetragonal symmetry, and as we increase the calcium content the symmetry changes to orthorhombic, as the level of oxygen vacancy ordering increases. Through Si doping there was consequently a decrease in the oxygen vacancy ordering and we observed an evolution to a cubic cell, where fully cubic symmetry is obtained at x=0.15 for y=0, 0.25 and 0.5. For higher Ca contents ($y \geq 0.75$), it does not, however, appear to be possible to stabilise the cubic cell symmetry at any silicon content under these ambient pressure synthesis conditions (see Fig. S1). The addition of higher levels of silicon in this series led to the segregation of secondary phases. In addition, it is worth mentioning that for samples with the same silicon content, those with higher strontium contents are closer to a cubic symmetry, see Fig. 2.

Unit cell parameters for these materials were determined from the X-ray diffraction data using the Rietveld method (see Table 1), and show an increase in the cell volume as the Si content increases. Similar results were reported in a previous work where $(Ca,Sr)MnO_3$-based compounds were successfully doped with silicon [39]. For this Mn system the change in cell parameters was explained by a balance between the effect of the smaller size of Si^{4+} (0.26 Å), which would be expected to lead to a reduction in cell volume, and the associated reduction of Mn^{4+} to give a greater concentration of Mn^{3+}, which would be expected to lead to an increase in cell volume. The formation of 3+ species through
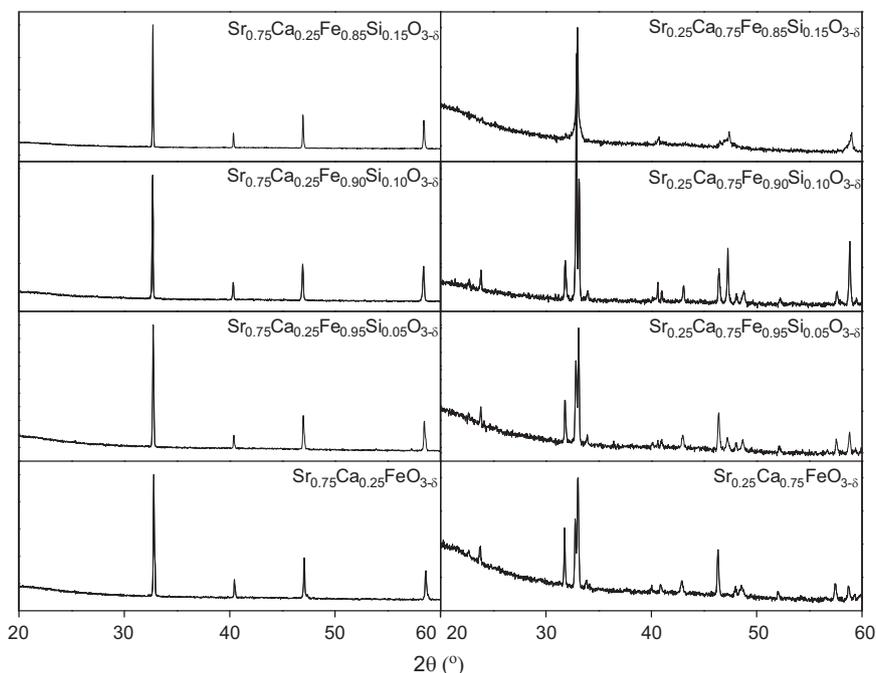
Fig. 1. X-ray diffraction patterns for: (left) $Sr_{0.75}Ca_{0.25}Fe_{1-x}Si_xO_{3-\delta}$ ($x=0$, 0.05, 0.10 and 0.15) and (right) $Sr_{0.25}Ca_{0.75}Fe_{1-x}Si_xO_{3-\delta}$ ($x=0$, 0.05, 0.10 and 0.15), showing the stabilization of the cubic form of these series through silicon doping. For the latter $Sr_{0.25}Ca_{0.75}Fe_{1-x}Si_xO_{3-\delta}$ phase, the stabilisation is not quite complete at 15% Si doping.
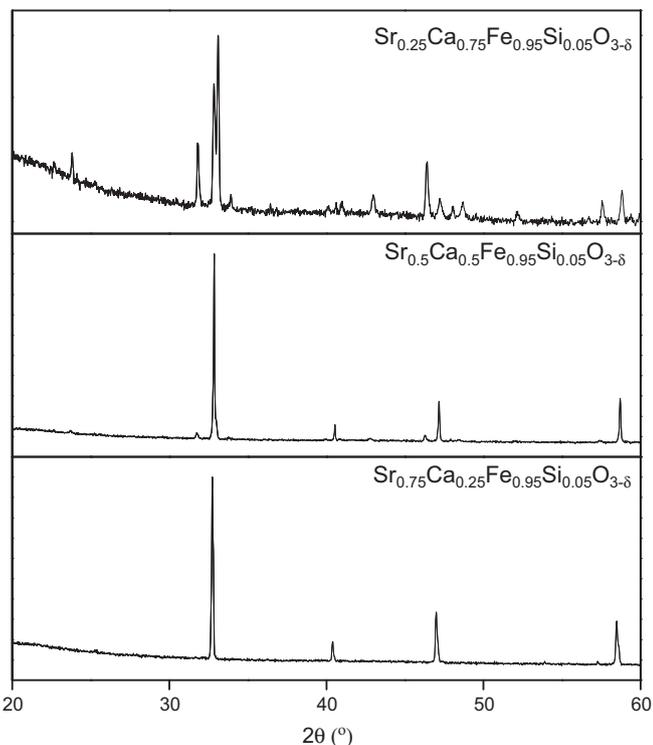
Fig. 2. X-ray diffraction patterns for (a) $Sr_{0.75}Ca_{0.25}Fe_{0.95}Si_{0.05}O_{3-\delta}$, (b) $Sr_{0.5}Ca_{0.5}Fe_{0.95}Si_{0.05}O_{3-\delta}$ and (c) $Sr_{0.25}Ca_{0.75}Fe_{0.95}Si_{0.05}O_{3-\delta}$, showing the effect of a low (5%) level of silicon doping at different strontium/calcium contents. At low Ca levels, this low level of Si is sufficient to stabilise the cubic cell, while as the Ca content increases, the appearance of extra peaks indicative of an orthorhombic cell is observed.

Si doping was predicted by the following defect equation, with the key driving force for the reduction of Mn^{4+} to Mn^{3+} being the introduction of oxide ion vacancies due to the lower coordination

(tetrahedral rather than octahedral) preference of the Si dopant:

$$SiO_2 + 3Mn^X_{Mn} + O^X_O \rightarrow Si^X_{Mn} + 2Mn'_{Mn} + V^{\cdot\cdot}_O + 1/2O_2 + \text{"}MnO_2\text{"} \qquad (1)$$
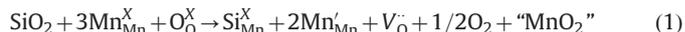
A similar explanation can be applied to the $Sr_{1-y}Ca_yFe_{1-x}Si_xO_{3-\delta}$ samples in the present study, with the introduction of oxide ion vacancies on Si incorporation favouring a reduction in the average Fe oxidation state. This is supported by the calculated average Fe oxidation states, reported in Table 2 (determined from the TGA studies), which showed a decrease in the average iron oxidation state and increase in the oxygen vacancies as the Si content increases. However, rather than mixed Fe^{4+}/Fe^{3+}, previous Mössbauer spectroscopy studies on $SrFe_{0.9}Si_{0.1}O_{3-\delta}$, showed that substitution of Fe^{4+} in $SrFeO_{3-\delta}$ by Si^{4+} induces disproportionation of the remaining Fe^{4+} into Fe^{3+} and Fe^{5+} [39], which was attributed to the smaller Si^{4+} causing significant local strain resulting in the Si^{4+} being surrounded by the large Fe^{3+} to relieve the strain with the adjacent cells incorporating the smaller Fe^{5+} ions. Whether a similar disproportionation is observed for the Ca doped samples requires further Mössbauer spectroscopy study of such systems.

As can be seen from the above equation, a key driving force for the reduction of Fe^{4+} to Fe^{3+} is the introduction of oxide ion vacancies due to the lower coordination (tetrahedral rather than octahedral) preference of the Si dopant (i.e. for $x=0$, the B cation site is completely occupied by Fe, while for $x > 0$ some Si is on this site, which will be tetrahedrally coordinated, and will thus lead to a reduction in the total oxygen content). Consequently, while we are nominally performing an isovalent (Si^{4+} in place of Fe^{4+}) substitution, the generation of oxide ion vacancies results in partial reduction, i.e. electron doping. This is confirmed, in good agreement with the defect equation given above.

3.2. Neutron diffraction structural study

The crystal structures of the $Sr_{1-y}Ca_yFe_{0.85}Si_{0.15}O_{3-\delta}$ series were refined for $y=0$, 0.25 and 0.5 samples, using neutron diffraction data. The data indicated a cubic cell (*Pm-3m*), with no

Table 1

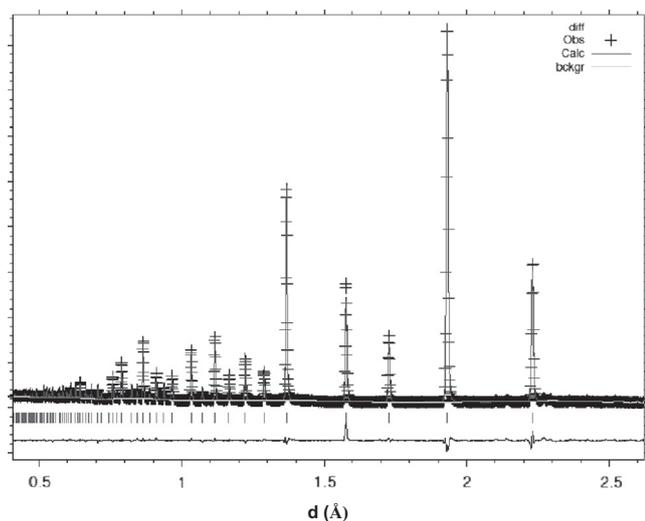Unit cell parameters and normalised cell volumes from XRD data for $Sr_{1-y}Ca_yFe_{1-x}Si_xO_{3-\delta}$. All the doped samples were refined in a cubic cell (Pm-$3m$), the undoped samples were refined in a tetragonal ($I4/mmm$) or orthorhombic ($Pcmn$) cell.

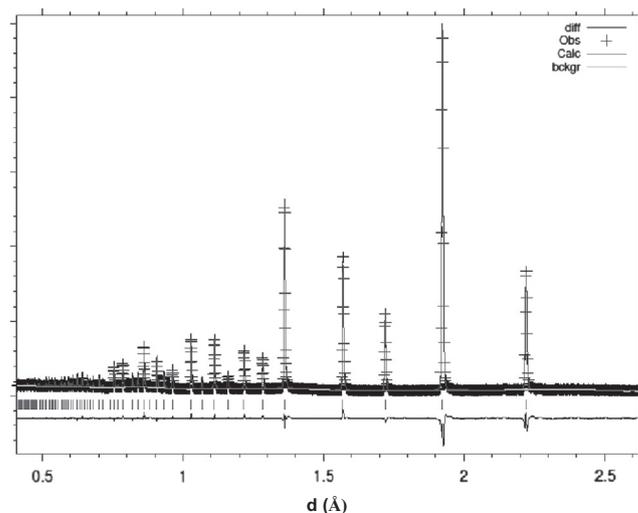| Ca (y)	0		0.25		0.5	
Si (x)	0	0.10	0	0.15	0	0.15
a (Å)	10.9235(1)	3.8723(1)	10.8895(1)	3.8619(1)	5.5828(1)	3.8415(1)
b (Å)	–	–	–	–	15.0433(1)	–
c (Å)	7.6965(1)	–	7.7083(1)	–	5.3991(1)	–
V/Z (Å³)	57.40(1)	58.06(1)	57.12(1)	57.60(1)	56.68(1)	57.21(1)

Table 2

Oxygen deficiencies (δ), Fe oxidation states (from TGA), conductivity data at 700 °C and ASR values at 800 °C in air for $Sr_{1-y}Ca_yFe_{1-x}Si_xO_{3-\delta}$ series. The error estimated for the oxygen deficiencies and iron oxidation states from the noise of the TGA line are ± 0.01 and ± 0.02, respectively.

	$Sr_{1-y}Ca_yFe_{1-x}Si_xO_{3-\delta}$					
Ca (y)	0		0.25		0.5	
Si (x)	0	0.10	0	0.15	0	0.15
Oxygen deficiency (δ)	0.10	0.23	0.12	0.18	0.14	0.17
Oxidation state	3.80	3.48	3.77	3.57	3.71	3.59
Conductivity at 700 °C (S cm⁻¹)	26.3	35.3	8.25	11.28	0.90	8.43
Conductivity at 800 °C (S cm⁻¹)	17.2	24.1	6.69	7.92	0.94	6.30
ASR at 700 °C (Ω cm⁻²)	1.65	0.90	0.91	0.51	2.30	0.93
ASR at 800 °C (Ω cm⁻²)	0.25	0.08	0.15	0.10	0.90	0.17

Fig. 4. Observed, calculated and difference neutron diffraction profiles for $Sr_{0.5}Ca_{0.5}Fe_{0.85}Si_{0.15}O_{3-\delta}$.

Fig. 3. Observed, calculated and difference neutron diffraction profiles for $Sr_{0.75}Ca_{0.25}Fe_{0.85}Si_{0.15}O_{3-\delta}$.

evidence for the presence of extra peaks indicative of oxide vacancy ordering (see Figs. 3 and 4). The $y=0.25$ sample did show the presence of a few very weak extra peaks, but these were not consistent with oxygen ordering models, and are most likely due to a small Si based impurity (($Sr/Ca)_2SiO_4$), since a Si content of 15% is at the limit of the solubility range. The refined structural data are shown in Table 3. For the refinement, the atomic displacement parameters for Sr and Ca and Fe and Si were constrained to be equal. The Sr and Ca and Fe and Si occupancies were refined, with the constraint that their sum equalled 1.0. The final values for the two pairs were in general agreement with those expected from the starting composition, as can be seen from Table 3. The oxygen atomic displacement parameters are higher than those of the other atoms which can be related to the local distortions caused by the presence of the silicate groups. If we compare the oxygen content obtained from TGA, 2.70, 2.82 and 2.86, and from neutron data, 2.69, 2.73 and 2.79, for $SrFe_{0.90}Si_{0.10}O_3$, $Sr_{0.75}Ca_{0.25}Fe_{0.85}Si_{0.15}O_3$ and $Sr_{0.5}Ca_{0.5}Fe_{0.85}Si_{0.15}O_3$,

respectively for both techniques, we can see a mismatch in the oxygen content for the calcium doped samples despite both set of data are following the same trend. The lower oxygen content for these samples from the neutron diffraction results may be due to local structural distortions, and accompanying oxygen displacements. In support of this, we can see that there is a significant worsening in the R_F values as the Ca content increases, despite the good fitting to the data overall. As stated earlier, for lower Si contents, the samples with more Ca are closer to an orthorhombic cell (Fig. 2). Therefore, at higher Ca contents the local environment may be more distorted despite the average cubic symmetry. In this respect, total scattering experiments to study the local structure of these samples would be of interest.
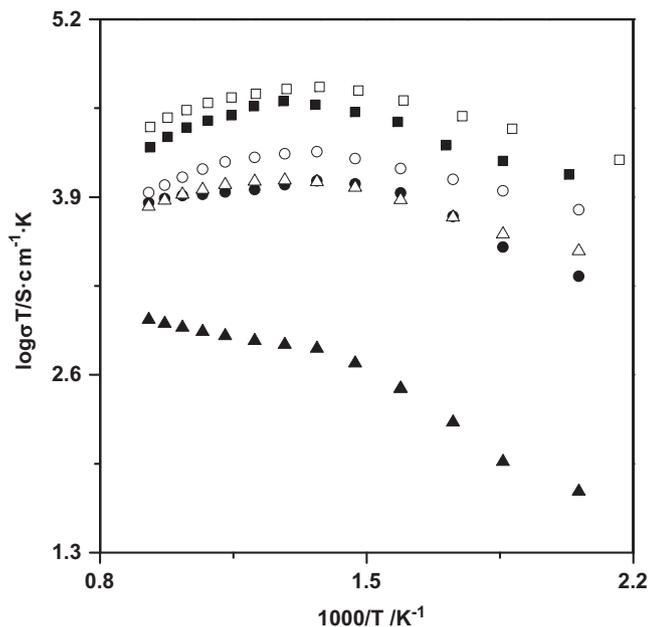
Overall, however, these results confirm the important role silicon doping plays in stabilising the cubic form in these ferrites, with no evidence found for long range oxide vacancy ordering.

3.3. Conductivity measurements

In this work, pellets for conductivity measurements were prepared at 1200 °C for 12 h, with densities for all the samples (doped and undoped) of $\sim$85%. Conductivities were initially measured for the undoped $Sr_{1-y}Ca_yFeO_{3-\delta}$ samples, which showed a small but significant decrease in conductivity, which can be attributed to an increasing distortion of the local environment on the introduction of Ca. For the Si doped series, $Sr_{1-y}Ca_yFe_{1-x}Si_xO_{3-\delta}$, samples containing the lowest level of Si to produce cubic symmetry were selected for conductivity measurements, i.e. $y=0$ $x=0.1$, and $y=0.25$ and 0.5 $x=0.15$. These data showed an increase in conductivity on Si doping (see Fig. 5). The % increase is most significant for the sample with the highest Ca content, where the undoped material shows a lower symmetry cell, indicating the strong beneficial effect from the higher

Table 3
Structural parameters (*Pm-3m* cubic cell) refined from neutron powder diffraction data for $Sr_{1-y}Ca_yFe_{1-x}Si_xO_{3-\delta}$ ($y=0$, 0.25 and 0.5, $x=0.10$, 0.15).

	$Sr_{1-y}Ca_yFe_{1-x}Si_xO_{3-\delta}$					
Ca (y)	*0*		*0.25*		*0.5*	
Si (x)	*0.10*		*0.15*		*0.15*	
a (Å)	3.8782(1)		3.8621(1)		3.8442(1)	
V (Å³)	58.33(1)		57.61(1)		56.81(1)	
Atom (x,y,z)	$U_{iso} \times 100$ (Å²)	*Occupancy*	$U_{iso} \times 100$ (Å²)	*Occupancy*	$U_{iso} \times 100$ (Å²)	*Occupancy*
Sr (0.5, 0.5, 0.5)	1.07(1)	1(−)	1.14(1)	0.79(1)	1.63(1)	0.56(1)
Ca (0.5, 0.5, 0.5)	–	–	1.14(1)	0.21(1)	1.63(1)	0.44(1)
Fe (0, 0, 0)	0.76(1)	0.92(1)	0.60(1)	0.89(1)	0.92(1)	0.89(1)
Si (0, 0, 0)	0.76(1)	0.08(1)	0.60(1)	0.11(1)	0.90(1)	0.11(1)
O (0.5, 0, 0)	1.64(1)	0.90(1)	2.62(1)	0.91(1)	0.90(1)	0.93(1)
R_{wp} (%)	3.73		3.19		4.63	
R_F (%)	1.16		4.30		4.57	
χ^2	5.08		15.08		26.00	

Fig. 5. Plot of $log\sigma$ vs. 1000/T for $SrFeO_{3-\delta}$ (■), $SrFe_{0.90}Si_{0.10}O_{3-\delta}$ (□), $Sr_{0.75}Ca_{0.25}$ $FeO_{3-\delta}$ (●), $Sr_{0.75}Ca_{0.25}Fe_{0.85}Si_{0.15}O_{3-\delta}$ (○), $Sr_{0.5}Ca_{0.5}FeO_{3-\delta}$ (▲) and $Sr_{0.5}Ca_{0.5}Fe_{0.85}$ $Si_{0.15}O_{3-\delta}$ (△).

Fig. 6. Plot of log (area-specific resistance (ASR)) vs. 1000/T for $SrFeO_{3-\delta}$ (■), $SrFe_{0.90}Si_{0.10}O_{3-\delta}$ (□), $Sr_{0.75}Ca_{0.25}FeO_{3-\delta}$ (●), $Sr_{0.75}Ca_{0.25}Fe_{0.85}Si_{0.15}O_{3-\delta}$ (○), $Sr_{0.5}Ca_{0.5}FeO_{3-\delta}$ (▲) and $Sr_{0.5}Ca_{0.5}Fe_{0.75}Si_{0.15}O_{3-\delta}$ (△).
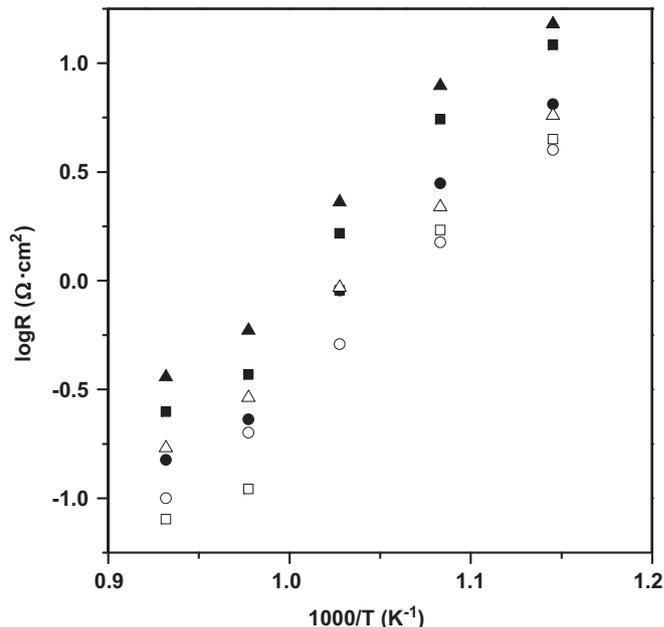
symmetry cubic cell. Another factor that will influence the conductivities is the observed changes in the Fe oxidation state. All samples showed a change in the conductivity plot above $\sim 400\,^\circ$C, due to oxygen loss at these higher temperatures reducing the Fe^{4+} content.

3.4. Area-specific resistance study

Following the conductivity results, cathode testing was performed for these samples. These experiments used a composite of the perovskite and CGO (1:1 wt%) on dense CGO10 pellets. The composite was deposited at 900 $^\circ$C, and at this temperature there was no evidence of any segregation of secondary phases in perovskite-CGO10 mixtures.

In Fig. S3, we show the impedance spectra for the symmetrical cells with SrFeO3/CGO10 and $SrFe_{0.90}Si_{0.10}O_{3-\delta}$/CGO10 cathodes. As can be seen, the arc is smaller for the Si-doped sample, which can be explained by the increase in electronic conductivity and likely also oxide ion conductivity (due to the generation of oxide ion vacancies caused by the oxyanion doping).

The dependencies of the ASR values in air with temperature are shown in Fig. 6 and Table 2. For instance, for $SrFe_{0.90}Si_{0.10}O_{3-\delta}$,

$Sr_{0.75}Ca_{0.25}Fe_{0.85}Si_{0.15}O_{3-\delta}$ and $Sr_{0.5}Ca_{0.5}Fe_{0.85}Si_{0.15}O_{3-\delta}$, the values obtained at 700 $^\circ$C, were 0.90, 0.51 and 0.93 Ω cm^{-2}, respectively. The results for the undoped samples, $SrFeO_{3-\delta}$, $Sr_{0.75}Ca_{0.25}FeO_{3-\delta}$ and $Sr_{0.5}Ca_{0.5}FeO_{3-\delta}$, were 1.65, 0.91 and 2.30 Ω cm^{-2}, respectively, indicating a significant improvement on Si doping. The ASR data show a non-linear behaviour with temperature, with a bigger decrease in the values at the higher temperatures. This behaviour is likely due to the fact that these systems show loss of oxygen at high temperature, causing an increase in oxide vacancies and hence a better oxide ion mobility and lower ASR values at the higher temperatures.

4. Conclusions

In $Sr_{1-y}Ca_yFe_{1-x}Si_xO_{3-\delta}$ perovskite materials with Ca contents $y \leq 0.5$, prepared by solid state reaction, powder neutron diffraction and X-ray diffraction data have shown that doping with silicon results in a change from tetragonal or orthorhombic symmetry, where the crystal structures contain ordered oxygen vacancies, to a cubic structure with disordered oxygen vacancies. With calcium contents higher than $y=0.5$ it was not possible the

stabilization of the cubic symmetry. An improvement in the conductivity is observed on Si doping due to the resultant modification of the Fe oxidation state and change to cubic symmetry. Composites with 50% $Ce_{0.9}Gd_{0.1}O_{1.95}$ were examined on dense $Ce_{0.9}Gd_{0.1}O_{1.95}$ pellets in air. An improvement in the area specific resistances (ASR) values is observed for the Si-doped samples. Thus these results reinforce the fact that silicon can be incorporated into perovskite materials and can have a beneficial effect on the performance, suggesting that its use as a dopant may be extended to other areas where perovskite systems are attracting interest.

Acknowledgments

Appendix A. Supporting information

Supplementary data associated with this article can be found in the online version at http://dx.doi.org/10.1016/j.jssc.2014.02.027.

References

[1] A. Orera, P.R. Slater, Chem. Mater. 22 (2010) 675–690.
[2] A.J. Jacobson, Chem. Mater. 22 (2010) 660–674.
[3] A. Lashtabeg, S.J. Skinner, J. Mater. Chem. 16 (2006) 3161–3170.
[4] A. Martínez-Amesti, A. Larranaga, L.M. Rodríguez-Martínez, A.T. Aguayo, J.L. Pizarra, M.L. Nóa, A. Laresgoiti, M.I. Arriortua, J. Power Sources 185 (2008) 401–410.
[5] D. Kuscer, D. Hanzel, J. Holc, M. Hrovat, Drago Kolar, J. Am. Ceram. Soc. 84 (2001) 1148–1154.
[6] C. Greaves, P.R. Slater, J. Mater. Chem. 1 (1) (1991) 17–21.
[7] C. Greaves, P.R. Slater, Physica C 175 (1991) 172–178.
[8] P.R. Slater, C. Greaves, M. Slaski, C.M. Muirhead, Physica C 208 (1993) 193–196.
[9] Y. Miyazaki, H. Yamane, N. Ohnishi, T. Kajitani, K. Hiraga, Y. Mori, S. Funahashi, T. Hirai, Physica C 198 (1992) 7–13.
[10] A. Maignan, M. Hervieu, C. Michel, B. Raveau, Physica C 208 (1993) 116–120.
[11] K. Kinochita, T. Yamada, Nature 357 (1992) 313–315.
[12] B. Raveau, M. Hervieu, D. Pelloquin, C. Michel, R. Retoux, Z. Anorg. Allg. Chem. 631 (2005) 1831–1839.
[13] D. Pelloquin, M. Hervieu, C. Michel, N. Nguyen, B. Raveau, J. Solid State Chem. 134 (1997) 395–408.
[14] V. Caignaert, B. Domenges, B. Raveau, J. Solid State Chem. 120 (1995) 279–289.
[15] C.A. Hancock, R.C.T. Slade, J. R Varcoe, P. R Slater, J. Solid State Chem. 184 (2011) 2972–2977.
[16] J.M. Porras-Vazquez, P.R. Slater, J. Power Sources 209 (2012) 180–183.
[17] J.M. Porras-Vazquez, T.F. Kemp, J.V. Hanna, P.R. Slater, J. Mater. Chem. 22 (2012) 8287–8293.
[18] D. Ivanova, E.M.C.L.G.P. Lima, A. Kovalevsky, F.M.L. Figueiredo, V.V. Kharton, F.M.B. Marques, Ionics 14 (2008) 349–356.
[19] X. Guo, R. Waser, Prog. Mater. Sci. 51 (2006) 151–210.
[20] M.J. Verkerk, A.J.A. Winnubst, A.J. Burggraaf, J. Mater. Sci. 17 (1982) 3113–3122.
[21] S.P.S. Badwal, J. Drennan, J. Mater. Sci. 22 (1987) 3231–3239.
[22] M.L. Mecartney, J. Am. Ceram. Soc. 70 (1987) 54–58.
[23] S.P.S. Badwal, J. Drennan, J. Mater. Sci. 24 (1989) 8896.
[24] D. Ivanova, A. Kovalevsky, V.V. Kharton, F.M.B. Marques, Bol. Soc. Esp. Ceram. Vidrio 47 (2008) 201–206.
[25] B.C.H. Steele, Solid State Ionics 129 (2000) 95–110.
[26] T.S. Zhang, J. Ma, S.H. Chan, P. Hing, J.A. Kilner, Solid State Sci. 6 (2004) 565–572.
[27] S.P.S. Badwal, Solid State Ionics 76 (1995) 67–80.
[28] J.M. Porras-Vazquez, P.R. Slater, Fuel Cells 12 (2012) 1056–1063.
[29] C.A. Hancock, P.R. Slater, Dalton Trans. 40 (2011) 5599–5603.
[30] J.M. Porras-Vazquez, E.R. Losilla, P.J. Keenan, C.A. Hancock, T.F. Kemp, J.V. Hanna, P.R. Slater, Dalton Trans. 42 (2013) 5421–5429.
[31] J. Yoo, A. Verma, S. Wang, A.J. Jacobson, J. Electrochem. Soc. 152 (2005) A497–A505.
[32] V. Zaspalis, A. Evdou, L. Nalbandian, Fuel 89 (2010) 1265–1273.
[33] Y. Niu, W. Zhou, J. Sunarso, L. Ge, Z. Zhu, Z. Shao, J. Mater. Chem. 20 (2010) 9619–9622.
[34] J.P. Hodges, S. Short, J.D. Jorgensen, X. Xiong, B. Dabrowski, S.M. Mini, C.W. Kimball, J. Solid State Chem. 151 (2000) 190–209.
[35] V. Vashuk, L. Kokhanovskii, I. Yushkevich, Inorg. Mater 36 (2000) 79–83.
[36] M.V. Patrakeev, I.A. Leonidov, V.L. Kozhevnikov, V.V. Kharton, Solid State Sci. 6 (2004) 907–913.
[37] P. Adler, A. Lebon, V. Damljanovicacute, C. Ulrich, C. Bernhard, A.V. Boris, A. Maljuk, C.T. Lin, B. Keimer, Phys. Rev. B: Condens. Matter 73 (2006) 094451.
[38] M. Schmidt, S.J. Campbell, J. Solid State Chem. 156 (2001) 292–304.
[39] J.M. Porras-Vazquez, T. Pike, C.A. Hancock, J.F. Marco, F.J. Berry, P.R. Slater, J. Mater. Chem. A 1 (2013) 11834–11841.
[40] T. Takeda, R. Kanno, Y. Kawamoto, M. Takano, S. Kawasaki, T. Kamiyama, F. Izumi, Solid State Sci. 2 (2000) 673–687.
[41] U. W Blass, F. Langenhorst, T. Boffa-Ballaran, F. Seifert, D.J. Frost, C.A. McCammon, Phys. Chem. Miner. 31 (2004) 52–65.
[42] M. Murakami, K. Hirose, K. Kawamura, N. Sata, Y. Ohishi, Science 304 (2004) 855–858.
[43] A.R. Oganov, S. Ono, Nature 430 (2004) 445–448.
[44] A.R. Oganov, R. Martonak, A. Laio, P. Raiteri, M. Parrinello, Nature 438 (2005) 1142–1144.
[45] A.C. Larson, R.B.V. Dreele, General Structure Analysis System (GSAS) program. Rep. no. LA-UR-86748, Los Alamos National Laboratory, Los Alamos, CA, 1994.
[46] D. Johnson, ZView: a Software Program for IES Analysis, Version 2.8, Scribner Associates, Inc. Southern Pines, NC, 2008.